

# Atomic Force Microscopy Control System for Electrostatic Measurements based on Mechanical and Electrical Modulation

Sergey Belikov, John Alexander, Sergei Magonov, and Ivan Yermolenko

*Abstract*— Atomic Force Microscopy (AFM) has excellent potential ability for quantitative electrostatic measurements of surface potential and dielectric permittivity of materials with nanoscale resolution. Implementation of this ability, however, requires overcoming several challenges. The first task is developing an accurate computational model for electrostatic tip-sample interaction; the second - efficient instrumentation and a control system that supports the measurements. An analytical model of nanoscale tip-sample capacitance on thin dielectric films was introduced (Gomila, Toset, and Fumagalli, 2008). This model allows describing the electrostatic tip-sample interaction force in a form suitable for the AFM dynamic control model (Belikov, Magonov, 2009). This dynamic model contains integrals over the tip-sample forces that can be presented in a closed form for the Gomila-Toset-Fumagalli analytical model. These results allow for developing very efficient electrostatic AFM computational model. As for the second task (instrumentation and control), the above mentioned AFM dynamic model with (amplitude-phase) state variables can be used for the control system design that combines mechanical Amplitude Modulation mode and consequent electrical modulation of the mechanical phase cosine. The cosine is monitored by lock-in amplifiers at the electrical modulation frequency, and twice that frequency; surface potential and dielectric permittivity of the sample can then be mapped. This paper presents the model derivation, description of instrumentation and control schematics, and their implementation on NT-MDT microscopes. Results are illustrated with practical measurements on different materials.

## I. INTRODUCTION

Local electrostatic force measurements in atomic force microscopy (AFM) have been introduced in 1988 [1]. Initially, Kelvin force microscopy (KFM) [2] was developed and it became an extension of macroscopic Kelvin probe measurements to small scale studies of different materials. The capacitance gradient  $dC/dZ$  can be also determined from electrostatic force studies by detecting the force response on the 2<sup>nd</sup> harmonic of the frequency of electric field excitation. This response has been utilized for mapping the local dielectric changes in a number of AFM-related methods [3-5], which were applied to semiconductor surfaces, thin organic films and water adsorbates on different surfaces. Recently, with broad development of multi-frequency techniques, KFM and  $dC/dZ$  mapping were expanded to studies of surface potential and dielectric permittivity of various materials and in different environments [6]. Enhanced sensitivity and high spatial resolution of the surface potential and capacitance gradient mapping have been demonstrated for semiconductors, metals, organic

materials and polymers. Recent results demonstrated that local electrical measurements are useful for compositional imaging of multi-component samples [7]. They essentially complement the similar applications of nanomechanical AFM studies. A more challenging task is the quantitative analysis of surface potential and dielectric data with the latter offering unique information about local molecular motion through studies at different frequencies and various temperatures. This capability led to increasing interest in the local dielectric studies of polymer samples in an attempt to bring dielectric spectroscopy to the sub-micron scale. Here we present an approach to a control system for extraction of quantitative dielectric permittivity from AFM electrostatic measurements on thin polymer films.

## II. BACKGROUND

### A. Background of AFM Asymptotic Dynamic and Quasi-Static Models

Asymptotic differential equations for the AFM mechanical dynamic modes such as Amplitude Modulation (AM) and Frequency Modulation (FM) were derived and studied in [8]. The full dynamic equations are presented in [8] and [9, formula (1)]. In this paper, however, we will need only the equations for steady state amplitude and phase, and conservative (i.e. with no dissipation) electrostatic tip-sample interaction forces. For the AM mode these quasi-static equations are the following [8]

$$\begin{cases} \sin \theta = A / A_0 \\ \cos \theta = -\frac{2Q_1}{\pi k A_0} \int_0^\pi F_z (Z_c + A \cos y) \cos y dy \end{cases} \quad (1)$$

where  $A$  and  $\theta$  are the steady state amplitude and phase of the AFM oscillation at the 1<sup>st</sup> eigenvalue frequency of the cantilever (in AM AFM mode  $A$  is kept near the set point amplitude under  $z$  servo feedback control);

$A_0$  is the free oscillation amplitude at the 1<sup>st</sup> resonance of the cantilever;

$Q_1$  is the quality factor of the cantilever at its first resonance;

$k$  is the spring constant of the cantilever;

$Z_c$  is the central position of the oscillating tip (i.e. height – controlled by  $z$ -servo);

and  $F_z$  is the  $z$ -projection of tip-sample interaction force.

Ref. [9] describes mechanical (elasto-adhesive) force modeling, while electrostatic models and their use in design of control system for electrostatic measurements is the main topic of this paper. The quasi-static model (1) is adequate for developing the quantitative measurements of this paper. The

full dynamic model, however, has a potential to significantly improve feedback control of dynamic AFM modes classified in [8,9].

### B. Background of Lock-In Amplifiers used with AFM

In AM mode the amplitude  $A$  and phase  $\theta$  of (1) can be detected by Lock-in Amplifiers. Functionally, Lock-in amplifiers measure the input signal at a specified reference frequency  $\omega_R$  using the reference signal  $A_R \sin(\omega_R t + \theta_R)$  with reference amplitude  $A_R$ , frequency  $\omega_R$  and phase  $\theta_R$ . The Lock-in outputs the following components of the monitored harmonics  $A \sin(\omega_R t + \theta)$  of the input signal:

$$\begin{aligned} \text{Amplitude} &= A; & \text{InPhase } X &= A \cos(\theta - \theta_R) \\ \text{Phase} &= \theta - \theta_R; & \text{Quadrature } Y &= A \sin(\theta - \theta_R) \end{aligned} \quad (2)$$

In this paper three Lock-ins will be used (Fig. 2):

- 1) "Lock-in  $\omega_m$ " monitors the measured deflection of the oscillating cantilever at its first mechanical resonance frequency  $\omega_m$
- 2) "Lock-in  $\omega_e$ " monitors the electrically modulated input at the frequency of electrical excitation  $\omega_e$  that will be defined later in the paper
- 3) "Lock-in  $2\omega_e$ " monitors the input at  $2\omega_e$ , as explained later.

### C. Background of Electrostatic AFM Modeling

The electrostatic AFM setting is shown in Fig. 1 [10]. In [10] the following formula for nanoscale capacitance with thin dielectric film was presented

$$C_{\text{apex}} = 2\pi\epsilon_0 R \ln \left\{ 1 + \frac{\tilde{R}}{z+p} \right\} + C_0(R, \theta_0) \quad (3)$$

Notations in (3) and their SI units in the brackets are the following:

$C_{\text{apex}}$ [F] is the capacitance between the tip and the substrate;

$\epsilon_0$ [F/m] is the vacuum dielectric constant

$\epsilon_r$ [1] is the relative dielectric permittivity of the film (used in Eq.(4));

$h$ [m] is the thickness of the film (used in Eq.(4));

$z$ [m] is the apex-film separation distance;

$R$ [m] is the effective apex radius;

$\theta_0$ [degree or rad] is the cone angle of the tip;

$\tilde{R} = R[1 - \sin \theta_0]$ ;

$$p = h / \epsilon_r \quad (4)$$

is the parameter that plays an important role in further development ( $p$  can be estimated from electrostatic measurements, but  $h$  should be measured independently to calculate  $\epsilon_r$ );

$C_0$ [F] is not important because in what follows we'll need only derivatives over  $z$  and this term does not depend on  $z$ .

Although derived empirically, formula (3) was validated in [10] with Finite Elements simulation and "demonstrated that the model is extremely accurate in a broad range of parameter values, including apex-film distance  $z$  from contact to 100nm, film thickness  $h$  from 1nm to 100nm,

relative dielectric constant  $\epsilon_r$  from 1 to 100, apex radius  $R$  from 30 to 200nm, and cone angles  $\theta_0$  from  $10^\circ$  to  $45^\circ$ ." With such a validation, formula (3) can be used for accurate analytical system development.

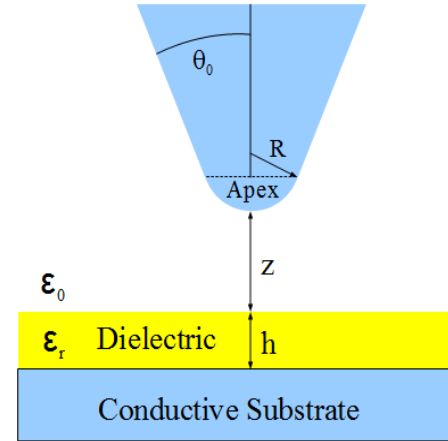


Fig. 1. A sketch of electrostatic set-up in AFM [10].

According to [10-11], only  $C_{\text{apex}}$  contribution depends on local material properties. As described in [11], another, long-range, contribution, called  $C_{\text{stray}}$ , is linear in  $z$ . This fact allows us to completely neglect this contribution if we use second derivative of the total capacitance or equivalent operator described later in the paper that eliminates the linear component.

The  $z$ -component of the electrostatic force acting on the tip and measured by AFM (assuming the cantilever spring constant is known) relates to the capacitance by the well-known formula from electrostatics:

$$F_z(z) = -\frac{1}{2} \frac{\partial C_{\text{apex}}}{\partial z} U^2 \quad (5)$$

where  $U$  is the voltage applied between the metallic tip and conductive substrate.

### D. Background of Kelvin Force Microscopy (KFM)

According to this method, an alternating low-frequency voltage  $U(t) = U_{\text{dc}} + U_{\text{ac}} \cos \omega_e t$  is applied between the tip and the substrate. Then, assuming  $C_{\text{apex}}$  in (5) does not depend on applied voltage,

$$F_z(z) = \quad (6)$$

$$-\frac{1}{2} C'_{\text{apex}}(z) \left[ U_{\text{dc}}^2 + \frac{U_{\text{ac}}^2}{2} \right] \quad (6, \text{dc})$$

$$-C'_{\text{apex}}(z) U_{\text{dc}} U_{\text{ac}} \cos \omega_e t \quad (6, \omega_e)$$

$$-\frac{1}{4} C'_{\text{apex}}(z) U_{\text{ac}}^2 \cos 2\omega_e t \quad (6, 2\omega_e)$$

The DC component (6, dc) of the measured force signal is difficult to separate from the background noise. However, Lock-ins can accurately detect  $\omega_e$  and  $2\omega_e$  components.

The DC component  $U_{\text{dc}}$  of  $U(t)$  in (6,  $\omega_e$ ) is the difference between the voltage  $U_{\text{tip}}$  applied to the tip and the local

surface potential  $U_{\text{sample}}$  (e.g. due to local dipole distribution or surface charges). Nullifying  $U_{\text{dc}}$ , i.e. the amplitude of  $\omega_e$ -harmonics by varying  $U_{\text{tip}}$ , the local surface potential can be measured:

$$U_{\text{sample}} = U_{\text{tip}}, \text{ when } \omega_e \text{ amplitude is nullified} \quad (7)$$

According to (6),  $2\omega_e$  amplitude is proportional to  $dC_{\text{apex}}/dz$  and can be used to derive the dielectric properties of the sample, e.g. permittivity  $\epsilon_r$ . Formula (3) is of great value for the derivation described in Section III.B.

### III. MODELING AND CONTROL SYSTEM

#### A. Diagram of AFM Control System for Electrostatic Measurements

The diagram is shown in Fig. 2. All drive signals (“AC Drive”, “ $U_{\text{ac}}$  Drive” and the references to the three Lock-ins) must be synchronized. To achieve this they are generated by direct digital synthesis in the same FPGA with the same clock source. “AC Drive” is also the reference to “Lock-in  $\omega_m$ ”, and “ $U_{\text{ac}}$  Drive” is also the reference to “Lock-in  $\omega_e$ ”. Digital Phase Shifters are used for initial manual tuning to nullify the in-phase X ( $\omega_m$ ) and quadrature Y ( $\omega_e$ ) components of corresponding Lock-ins.

The  $\omega_m$ -phase shifter is tuned when the cantilever is at free oscillation at or near its resonance frequency far from the surface so there is neither mechanical nor electrostatic interaction. In this case  $\theta = \theta_m \approx \pi/2$  after the tuning.

The  $\omega_e$ -phase shifter is tuned after the tip is engaged and Tip Bias Voltage applied. Because we do not know the surface potential of an unknown sample, and therefore do not know if the potential difference between tip and sample is positive or negative, a bias  $U_{\text{dc}} = U_{\text{tip}} - U_{\text{sample}}$  significantly larger than the maximum expected difference is applied during the phase adjustment process. The  $\omega_e$ -phase shifter is tuned to maximize the X component of “Lock-in  $\omega_e$ ” with the large fixed  $U_{\text{dc}}$  value.

Now, after tuning, the  $\omega_e$ -modulated X component of “Lock-in  $\omega_m$ ”  $A \cos(\theta)$  is the input to “Lock-in  $\omega_e$ ”. Its X component (that can be positive or negative) is the error input to the “KFM Servo” that nullifies it by controlling  $U_{\text{tip}}$  (“DC Servo”). According to Eq. (6,  $\omega_e$ ) and (7), in this case

$U_{\text{tip}}$  provides the value of the surface potential.

Without the “Tip Bias Voltage”, the diagram of Fig. 2 is a typical AM AFM mode. The cantilever is vibrating at its mechanical resonance frequency  $\omega_m$  by “AC Drive  $\omega_m$ ”. “AC Deflection”, measured by the “Photo Detector” is locked in at the frequency  $\omega_m$ . “Lock-in  $\omega_m$ ” outputs the amplitude  $A$  and phase  $\theta$  modeled by Eq. (1). Amplitude  $A$  is an input to the “Z Servo” that is tracking a given set-point amplitude. For a steady-state amplitude  $A$ , corresponding steady-state phase can be calculated by the first equation of (1). For the best electrostatic performance  $A$  should be as close to  $A_0$  as possible to minimize mechanical force but still must track the topography of the sample. In this case  $\theta_m \approx \pi/2$  (subscript  $m$  indicates that this is mechanical phase that is not electrically modulated).

When electrically modulated “Tip Bias Voltage” is applied, phase  $\theta(t) = \theta_m + \Delta\theta_e(t)$  and  $\cos\theta(t) \approx -\Delta\theta_e(t)$ , because  $\theta_m \approx \pi/2$ . This shows that phase cosine change is due to the electrical modulation, and we can use components of the  $\cos\theta(t)$  in further derivations of dielectric permittivity. From the second equation of (1) and (6,  $\omega_e$ ), (6,  $2\omega_e$ ), the  $\omega_e$  and  $2\omega_e$  amplitudes of the phase cosines are the following:

$$G_{\omega_e}^{\cos\theta} = \frac{2Q_1 U_{\text{dc}} U_{\text{ac}}}{\pi A_0 k} \int_0^\pi C'_{\text{apex}} (Z_c + A \cos y) \cos y dy \quad (8)$$

$$G_{2\omega_e}^{\cos\theta} = \frac{Q_1 U_{\text{ac}}^2}{2\pi A_0 k} \int_0^\pi C'_{\text{apex}} (Z_c + A \cos y) \cos y dy \quad (9)$$

Statement 1 in the Appendix proves that the integral in (8) and (9) is non-negative, and so the right parts are valid expressions for the amplitudes.

The “Lock-in  $\omega_e$ ” and “KFM Servo” eliminate  $G_{\omega_e}^{\cos\theta}$  by nullifying  $U_{\text{dc}}$  according to the KFM technique outlined above and implemented as shown in Fig. 2. The next section uses Eq. (9) for mapping dielectric permittivity of the sample using the “Amplitude” output of the “Lock-in  $2\omega_e$ ”.

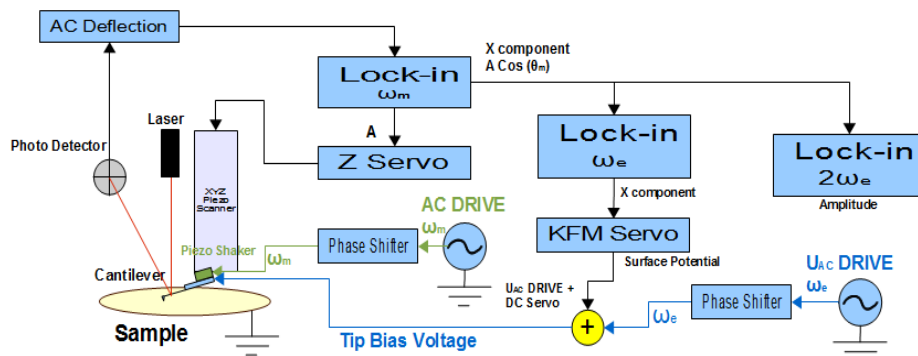


Fig. 2. Diagram of the Electrostatic AFM Control System with mechanical and electrical modulation

B. Derivation and Mapping of Relative Dielectric Permittivity  $\epsilon_r$  from the Experimental Measurements

It is convenient to use the following notations

$$C = \frac{C_{\text{apex}} \tilde{R}}{2\pi\epsilon_0 R}; \quad x = \frac{\tilde{R}}{z+p}; \quad (10)$$

$$\frac{dx}{dz} = -\frac{\tilde{R}}{(z+p)^2} = -\frac{x^2}{\tilde{R}}$$

Then derivatives of  $C$  are the following:

$$C' = \frac{dC}{dz} = -\frac{x^2}{1+x}; \quad x \geq 0 \Rightarrow C' < 0 \quad (11)$$

$$C'' = \frac{d^2C}{dz^2} = \frac{1}{\tilde{R}} \cdot \frac{x^4 + 2x^3}{(1+x)^2}; \quad x \geq 0 \Rightarrow C'' \geq 0 \quad (12)$$

Using expression for  $C$  in (10), Eq. (9) can be written as

$$\frac{A_0 k \tilde{R}}{Q_1 U_{ac}^2 \epsilon_0 R} [G_{2\omega_e}^{\cos\theta}] = \int_0^\pi C'(Z_c + A \cos y) \cos y dy \quad (13)$$

Statement 1 in the Appendix proves that the integral is non-negative. The last integral in the proof also reveals that contributions to the capacitance, which are linear with respect to  $z$ , such as  $C_{\text{stray}}$  mentioned in section I.C, are eliminated – which is an important advantage of the described method. Statement 2 in the Appendix derives an analytical expression for the integral in (13) using  $x$  and  $\bar{A}$  in (16) and  $C'(z)$  in (11). The expression is valid for

$$A \leq Z_c + p \quad (14)$$

where  $p$  is defined in (4). Inequality (14) is a natural restriction on the amplitude  $A$ . Using this expression, equation (13) can be written as

$$\begin{aligned} [G_{2\omega_e}^{\cos\theta}] &= \frac{2A_0 k \tilde{R}}{\pi Q_1 U_{ac}^2 \epsilon_0 R \bar{A}} \\ &= \frac{2}{\bar{A}^2} \left[ \frac{1}{\sqrt{1 - \bar{A}^2 x^2}} - \frac{1+x}{\sqrt{(1+x)^2 - \bar{A}^2 x^2}} \right] \quad (15) \end{aligned}$$

where

$$\bar{A} = A/\tilde{R}; \quad x = \frac{\tilde{R}}{Z_c + p}; \quad p = \frac{h}{\epsilon_r} \quad (16)$$

( $p$  was defined in (4)).

Statement 3 in the Appendix proves that equation (15) has a unique solution  $x \in ]0, \bar{A}^{-1}[$  and the function at (15, RHS) is monotonically increasing. This allows us to use the Newton-Raphson method [12] to find  $x$ . The computations demonstrated excellent convergence.

After finding  $x$ , the relative dielectric permittivity can be calculated from (16) assuming that  $h$  is measured:

$$\epsilon_r = \frac{h}{\tilde{R}/x - Z_c} \quad (17)$$

The described calculations are simple enough to be implemented on-line for mapping surface potential and

relative dielectric permittivity of the sample. Ref. [13] describes methods to evaluate the required parameters of the cantilever.

IV. EXPERIMENTAL MEASUREMENTS

A practical example of KFM and local dielectric measurements is taken from studies of two polymers: poly(styrene) – PS, poly(vinyl acetate) – PVAC and their blend. An NTEGRA-PRIMA microscope (NT-MDT) was used in this study.

The polymers exhibit different electric and dielectric properties. PVAC chains have a stronger dipole moment of 2.1D compared to those of PS (0.3D). At room temperature dielectric permittivity  $\epsilon_r$  of PVAC varies from 2.5 to 8 depending on frequency, whereas  $\epsilon_r$  of PS is around 2 and does not depend on frequency [14]. For AFM studies we prepared thin films of these polymers and their symmetric blend by spin-casting their dilute solutions in toluene on conducting ITO glass. The films' thickness  $h$  was determined by measuring the height of a scratch made in the films with a sharpened wood stick. The latter is rigid enough to abrade the polymer without damage to the substrate. The scratch locations of the neat films were also examined for detection of the changes of the cosine amplitude signal (at  $2\omega_e$ ) on the film and substrate. The amplitude changes were recorded at AC bias voltage in the 0-2.5V range at a frequency of 4 kHz. The AFM measurements of the sample topography and local dielectric properties were performed with conducting Pt-coated Si probes, which have stiffness 2-3 N/m and different tip shape (cone angle 17.5 and 20 degrees) and apex radii (15 nm and 30 nm). The scan speed was selected 0.6 Hz (i.e. 0.6 512-pixel lines per second).

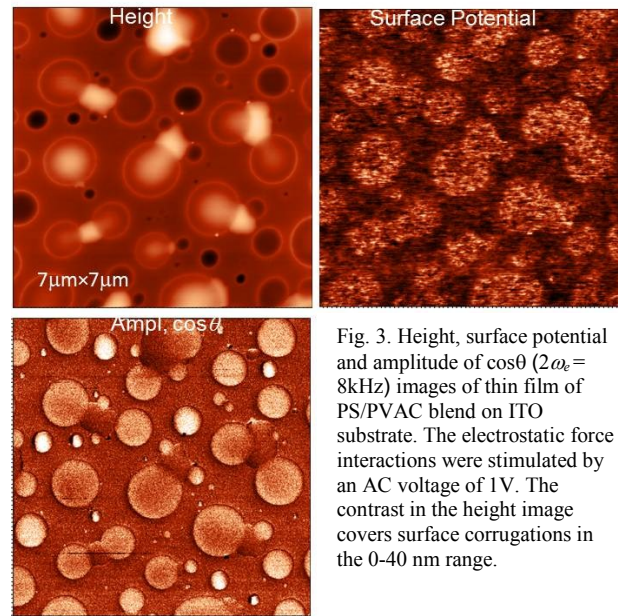


Fig. 3. Height, surface potential and amplitude of  $\cos\theta$  ( $2\omega_e = 8\text{kHz}$ ) images of thin film of PS/PVAC blend on ITO substrate. The electrostatic force interactions were stimulated by an AC voltage of 1V. The contrast in the height image covers surface corrugations in the 0-40 nm range.

The AFM topography and surface potential image of thin film of PS/PVAC blend are shown in Fig. 3 together with the map of cosine amplitude recorded at  $2\omega_e=8\text{kHz}$ . The surface of this film is characterized by round-shape

domains imbedded into a matrix. Elevated rims are seen around the domains, whose internal part has different z-levels. The morphology is consistent with the immiscible nature of this PS/PVAC blend. Several protruded patches seen between the elevated domains were formed as a result of the film annealing above glass transition temperature of PVAC. Most likely these patches resulted from a viscous flow of this polymer from the nearby domains. The observations as well as the binary contrast of the surface potential image indicate that the rounded domains are enriched in PVAC and the matrix is mostly formed of PS. This suggestion has been confirmed by combined AFM and confocal Raman studies, where PVAC-sensitive bands were recorded at the domains' locations. In contrast to the surface potential image that differentiates the blend constituents due to differences in molecular dipole of the PS and PVAC chains, the map of amplitude cosine exhibits a rather complicated contrast. The latter has some resemblance with the sample topography that might reflect the dependence of cosine amplitude on the ratio of sample thickness to permittivity:  $p = h/\epsilon_r$ . Therefore, the analysis of the cosine amplitude image is not straightforward and the extraction of the permittivity map from these data requires additional efforts.

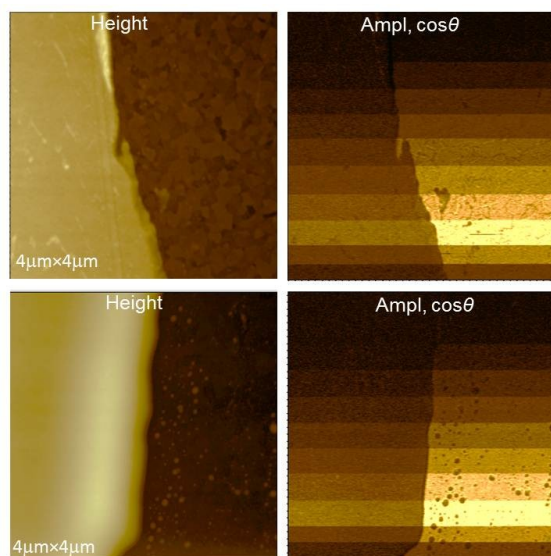


Fig. 4. Height and cosine amplitude images obtained at the scratch locations on PS (top) and PVAC (bottom) films on ITO. The evaluated film thickness is  $\sim 160$  nm for PS and  $\sim 150$  nm for PVAC. In amplitude images, the changes reflect the variations of AC bias voltage (from top to bottom) from 0 to 2V in increments of 0.25 and the last two voltages were reduced to 1.5V and 1.0 V. Amplitude  $\cos\theta$  range is 0-0.0056.

As the first step in this direction we conducted the local dielectric measurements at the scratch locations of PS and PVAC films, Fig. 4. The films' surfaces, which are seen in the left part of the height images, are relatively smooth and featureless. The grainy morphology of ITO substrate is best seen in the right side of the height image of PS. In case of PVAC sample, the substrate surface is partially covered by multiple polymer particles. The amplitude cosine images distinctively reveal the contrast variations between the

polymer films and ITO substrate. For both materials, the amplitude increases with AC bias voltage and in the detailed report we will show that the experimental data well match the quadratic dependence of amplitude on AC bias voltage, particularly at the voltages in the 0.75V-2.0V range. Therefore, we collected the results of permittivity calculations for the experimental amplitude cosine values obtained for AC bias of 1V, Table 1.

TABLE 1.  
Calculated Dielectric Permittivity for Thin Films of PS and PVAC.

Amplitude	6 nm	18 nm	48 nm	19 nm	38 nm	76 nm
$\epsilon_r$ (PS)	1.13	1.33	1.71	1.65	1.67	1.68
$\epsilon_r$ (PVAC)	1.80	1.90	2.18	2.36	2.25	2.30
$\epsilon_r(\text{PVAC})/\epsilon_r(\text{PS})$	1.59	1.43	1.27	1.43	1.35	1.37

The experiments were conducted at several oscillation amplitudes with conducting probes having nominal apex radii of 15nm and 30nm. The calculated permittivity values are consistent with macroscopic dielectric data on these materials. Although the absolute  $\epsilon_r$  values depend on the tip radius and applied oscillation amplitudes, the ratio of dielectric permittivity of PS versus PVAC shows much less variability. The obtained results can be considered as strong support for the applied theoretical model.

In the expansion of the theoretical analysis to the PS/PVAC film, we consider its columnar model structure in Fig. 5. The constructed cosine amplitude profile, which is based on the obtained permittivity data, is shown above the corrugated surface of the model. There is definite similarity of these profiles with the experimental images in Fig. 3.

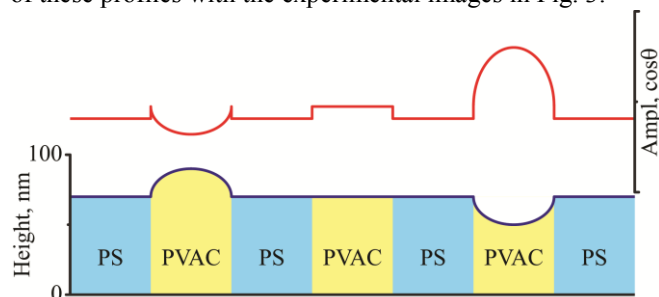


Fig. 5. A model of thin PS/PVAC film and the amplitude  $\cos\theta$  profile above. The profile was calculated using the permittivity data extracted from the studies of the neat polymer films.

## V. CONCLUSION

AFM-based local studies of electric and mechanical properties benefit from multi-frequency approaches. This statement is illustrated by measurements of the mechanical cosine phase changes induced by tip-sample electrostatic forces related to local dielectric permittivity. The extraction of quantitative dielectric permittivities for thin polymer films shows definite correlations with the macroscopic data.

Control system design based on asymptotic nonlinear

AFM dynamics (or rather quasi-statics in this paper) combined with multi-frequency modulation (mechanical and electrical) proved efficient and will be extended.

Analytical derivations, especially simple expression of the integral in (1) for electrostatic force model, make related computations simple enough for electrostatic property mapping as well as for efficient simulations.

#### APPENDIX

**Statement 1.** Integral in (8) and (9) is non-negative, i.e.

$$\int_0^{\pi} C'_{\text{apex}}(Z_c + A \cos y) \cos y dy \geq 0$$

**Proof.** The integral is equal to

$$\begin{aligned} & \int_0^{\pi/2} C'_{\text{apex}}(Z_c + A \cos y) \cos y dy + \\ & \int_{\pi/2}^{\pi} C'_{\text{apex}}(Z_c + A \cos y) \cos y dy = \\ & \int_0^{\pi/2} [C'_{\text{apex}}(Z_c + A \cos y) \cos y + \\ & C'_{\text{apex}}(Z_c + A \cos(\pi - y)) \cos(\pi - y)] dy = \\ & \int_0^{\pi/2} [C'_{\text{apex}}(Z_c + A \cos y) - C'_{\text{apex}}(Z_c - A \cos y)] \cos y dy \end{aligned}$$

According to (10) and (12), the derivative of  $C'_{\text{apex}}$  is non-negative. Then, due to monotonicity of  $C'_{\text{apex}}$ , the expression under the last integral is non-negative and the statement is proved.

**Statement 2.** If inequality (14) holds, the integral in (13) can be calculated by the formula

$$I = \int_0^{\pi} C'(Z_c + A \cos y) \cos y dy = \frac{\pi}{A} \left[ \frac{1}{\sqrt{1 - \bar{A}^2 x^2}} - \frac{1+x}{\sqrt{(1+x)^2 - \bar{A}^2 x^2}} \right]$$

where  $x$  and  $\bar{A}$  are calculated by formula (16).

**Proof.** Using the expression for  $C'(z)$  defined in (10)-(11),

$$I = \int_0^{\pi} \frac{\tilde{R}^2 \cos y dy}{(A \cos y + Z_c + p)(A \cos y + Z_c + p + \tilde{R})}$$

The function under the integral is rational with respect to  $\cos y$ , and using standard change of variables  $t = \tan(y/2)$ ,

$$I = -2\tilde{R}^2 \times \int_0^{\infty} \frac{(1-t^2) dt}{[t^2(Z_c + p - A) + (Z_c + p + A)][t^2(Z_c + p + \tilde{R} - A) + (Z_c + p + \tilde{R} + A)]}$$

When inequality (14) holds, the integral can be calculated by standard calculus methods,

$$I = \frac{\pi \tilde{R}}{A} \left[ \frac{Z_c + p}{\sqrt{(Z_c + p)^2 - A^2}} - \frac{Z_c + p + \tilde{R}}{\sqrt{(Z_c + p + \tilde{R})^2 - A^2}} \right]$$

and expressed in terms of variables in (16) to conclude the proof.

**Statement 3.** Equation (15) for any positive LHS has a unique solution  $x \in ]0, \bar{A}^{-1}[$ .

**Proof.** Derivative of (15, RHS)

$$\begin{aligned} & \frac{d}{dx} \left\{ \frac{2}{A^2} \left[ \frac{1}{\sqrt{1 - \bar{A}^2 x^2}} - \frac{1+x}{\sqrt{(1+x)^2 - \bar{A}^2 x^2}} \right] \right\} = \\ & 2x \left[ \frac{1}{(1 - \bar{A}^2 x^2)^{3/2}} - \frac{1}{((1+x)^2 - \bar{A}^2 x^2)^{3/2}} \right] > 0 \end{aligned}$$

is positive because for a positive  $x$ , the second expression in the latest brackets is smaller than the first one. This monotonicity guarantees the uniqueness of the solution of equation (15). The existence of the solution follows from the fact that function (15, RHS) is equal to zero at  $x=0$  and goes to infinity as  $x \rightarrow \bar{A}^{-1}$ .

#### REFERENCES

- [1] Y. Martin, D. A. Abraham, and H. K. Wickramasinghe "High-resolution capacitance measurement and potentiometry by force microscopy" *Appl. Phys. Lett.* 1988, 52, pp. 1103–10005.
- [2] M. Nonnenmacher, M. P. O'Boyle, and H. K. Wickramasinghe "Kelvin probe force microscopy" *Appl. Phys. Lett.* 1991, 58, pp. 2921–2923.
- [3] H. Yokoyama, and M. J. Jeffery "Imaging high-frequency dielectric dispersion of surfaces and thin films by heterodyne force-detected scanning Maxwell stress microscopy" *Colloids Surf. A* 1994, 93, pp. 359–373.
- [4] M. Fujihira "Kelvin probe force microscopy of molecular surfaces" *Annu. Rev. Mater. Sci.* 1999, 29, pp. 353–380.
- [5] M. Salmeron, "Scanning Polarization Force Microscopy. A Technique for Studies of Wetting Phenomena at the Nanometer Scale," *Oil Gas Sci Technol.* 2001, 56, pp. 63-75.
- [6] S. Magonov, J. Alexander, and S. Wu "Advancing Characterization of Materials with Atomic Force Microscopy-Based Electric Techniques" in "Scanning probe microscopy of functional materials" Eds. S. Kalinin and A. Gruverman, Chapter 9, pp. 233-300, 2011, Springer.
- [7] S. Magonov and J. Alexander "Single-pass Kelvin force microscopy and dC/dZ measurements in the intermittent contact: applications to polymer materials," *Beilstein Jour. Nanotech.* 2011, 2, pp. 15-27.
- [8] S. Belikov and S. Magonov, "Classification of Dynamic Atomic Force Microscopy Control Modes Based on Asymptotic Nonlinear Mechanics," in Proceedings of 2009 American Control Conference, pp. 979-984.
- [9] S. Belikov and S. Magonov, "Tip-Sample Interaction Force Modeling for AFM Simulation, Control Design, and Material Property Measurement," in Proceedings of 2011 American Control Conference, pp. 2867-2872.
- [10] G. Gomila, J. Toset, and L. Fumagalli, "Nanoscale capacitance microscopy of thin dielectric films," *Journal of Applied Physics*, vol. 104, 2008, pp. 024315 1-8
- [11] L. Fumagalli, G. Ferrari, M. Sampietro, and G. Gomila, "Dielectric constant measurement of thin insulating film at low frequency by nanoscale capacitance microscopy," *Applied Physics Letters*, vol. 91, 2007, pp. 243101 1-3.
- [12] W. Press, S. Teukolsky, W. Vetterling, and B. Flannery, *Numerical Recipes*, Cambridge Univ. Press, 2007.
- [13] S. Belikov et al, "Parametrization of atomic force microscopy tip shape models for quantitative nanomechanical measurements," *J. Vac. Sci. Technol. B* 27(2), 2009, pp. 984-992.
- [14] J. Sunga, S. Park, J. Park, H. Choi, and J. Choi, "Characteristics of poly(vinyl acetate) as a gate insulating material in organic thin film transistors," *Synthetic Metals*, 156, 2006, pp. 861–864.